

Article

Visible Light Trapping against Charge Recombination in FeO_x-TiO₂ Photonic Crystal Photocatalysts

Martha Pylarinou ¹, Alexia Toumazatou ¹, Elias Sakellis ², Evangelia Xenogiannopoulou ², Spiros Gardelis ¹, Nikos Boukos ², Athanasios Dimoulas ² and Vlassis Likodimos ^{1,*}

¹ Section of Condensed Matter Physics, Department of Physics, University Campus, National and Kapodistrian University of Athens, 15784 Athens, Greece; pylarin@phys.uoa.gr (M.P.); alextoug@phys.uoa.gr (A.T.); sgardelis@phys.uoa.gr (S.G.)

² Institute of Nanoscience and Nanotechnology, National Center for Scientific Research “Demokritos”, 15341 Agia Paraskevi, Greece; e.sakellis@inn.demokritos.gr (E.S.); e.xenogiannopoulou@inn.demokritos.gr (E.X.); n.boukos@inn.demokritos.gr (N.B.); a.dimoulas@inn.demokritos.gr (A.D.)

* Correspondence: vlikodimos@phys.uoa.gr; Tel.: +30-210-727-6824

Abstract: Tailoring metal oxide photocatalysts in the form of heterostructured photonic crystals has spurred particular interest as an advanced route to simultaneously improve harnessing of solar light and charge separation relying on the combined effect of light trapping by macroporous periodic structures and compositional materials’ modifications. In this work, surface deposition of FeO_x nanoclusters on TiO₂ photonic crystals is investigated to explore the interplay of slow-photon amplification, visible light absorption, and charge separation in FeO_x-TiO₂ photocatalytic films. Photonic bandgap engineered TiO₂ inverse opals deposited by the convective evaporation-induced co-assembly method were surface modified by successive chemisorption-calcination cycles using Fe(III) acetylacetonate, which allowed the controlled variation of FeO_x loading on the photonic films. Low amounts of FeO_x nanoclusters on the TiO₂ inverse opals resulted in diameter-selective improvements of photocatalytic performance on salicylic acid degradation and photocurrent density under visible light, surpassing similarly modified P25 films. The observed enhancement was related to the combination of optimal light trapping and charge separation induced by the FeO_x-TiO₂ interfacial coupling. However, an increase of the FeO_x loading resulted in severe performance deterioration, particularly prominent under UV-Vis light, attributed to persistent surface recombination via diverse defect d-states.

Keywords: photonic crystals; titanium dioxide; iron oxides; photocatalysis; slow photons



Citation: Pylarinou, M.; Toumazatou, A.; Sakellis, E.; Xenogiannopoulou, E.; Gardelis, S.; Boukos, N.; Dimoulas, A.; Likodimos, V. Visible Light Trapping against Charge Recombination in FeO_x-TiO₂ Photonic Crystal Photocatalysts. *Materials* **2021**, *14*, 7117. <https://doi.org/10.3390/ma14237117>

Academic Editor: Alina Pruna

Received: 22 October 2021

Accepted: 19 November 2021

Published: 23 November 2021

Publisher’s Note: MDPI stays neutral with regard to jurisdictional claims in published maps and institutional affiliations.



Copyright: © 2021 by the authors. Licensee MDPI, Basel, Switzerland. This article is an open access article distributed under the terms and conditions of the Creative Commons Attribution (CC BY) license (<https://creativecommons.org/licenses/by/4.0/>).

1. Introduction

Simultaneous enhancement of light-harvesting and photogenerated charge separation has been a major requisite for the development of advanced semiconductor photocatalysts and their deployment for solar energy conversion applications using environmentally benign materials [1,2]. Augmenting light utilization has been intensely pursued by rational materials’ design [3], especially for the benchmark titania (TiO₂) photocatalysts [4,5], ranging from electronic bandgap and defect engineering by doping [6,7], compositing with plasmonic [8,9], narrow bandgap semiconducting [10,11] as well as graphene-based [12,13] nanomaterials. A promising, though the challenging approach to intensify light-matter interactions and amplify photon capture is based on the fabrication of photocatalytic photonic crystals (PCs), i.e., periodically ordered structures, whose refractive index is spatially modulated on the scale of light’s wavelength [14–17]. PC-assisted photocatalysis has been accordingly put forward as an advanced structural modification that may selectively improve light trapping at frequencies of weak materials’ electronic absorption, by retarding light propagation at the edges of the fundamental photonic bandgap (PBG) [18] and higher

frequency photonic bands [19] as well as by multiple light scattering due to the persistent disorder and imperfections in PCs [20]. Besides extending the optical path of incident photons, PC structures, the most common being inverse opals as well as periodically ordered alumina and GaN structures tailored by electrochemical anodization [21–23], provide a macroporous scaffold that along with the secondary mesoporosity of its inorganic skeleton lead to a network of interconnected macro-mesopores [24], which facilitate reactants adsorption and diffusion during the photocatalytic process [25]. Substantial research has been thus devoted to exploiting these advantageous characteristics in combination with materials' compositional properties in order to develop visible light-activated (VLA) photonic photocatalysts [26], including coupling PCs with plasmonic [27–30] and graphene nanomaterials [31–33] as well as metal-oxide (MO) nanoclusters [34–36].

In particular, titania's surface modification by nanoscale MOs has been attracting significant attention as a versatile method for solar light photocatalytic applications via MOs' action as VLA sensitizers that also promote charge separation via interfacial charge transfer [37–41] and/or co-catalysts of TiO₂ [42–44]. Among the different MOs, nanostructured iron oxides, especially hematite α -Fe₂O₃, have been drawing continuous interest for VLA photocatalysis due to their ample earth abundance, narrow bandgap, nontoxicity, and low cost [45]. Despite limitations due to the inherently poor electrical conductivity, short diffusion lengths, and fast recombination that impair the photocatalytic activity of iron oxides (FeO_x) [46], compositing with titania has shown promising results for organic pollutant decomposition and water splitting under favorable FeO_x–TiO₂ interfacial coupling that enables efficient charge separation [47–52], especially under visible light [53,54]. Composite Fe₂O₃/TiO₂ semiconductors under UV and/or visible light, may cause interparticle charge transfer from TiO₂ to Fe₂O₃ nanoparticles since both the valence and conduction bands of ferric oxides to lie within titania's bandgap [55], frequently leading to performance deterioration for the coupled system because of the weaker photocatalytic activity of Fe₂O₃. Controlled grafting of nanoscale Fe₂O₃ clusters on titania's surface has been performed by Tada et al. [56] employing iron acetylacetonates' chemisorption on TiO₂ followed by post-calcination [57], featuring the chemisorption-calcination-cycle (CCC) technique that was successfully applied for the deposition of various MOs on TiO₂ [37]. Thorough investigations of Fe₂O₃–surface-modified TiO₂ have shown that high photocatalytic activity could be attained via Fe–O–Ti interfacial bonds inducing d-surface states, which raise the valence band of titania circumventing the unfavorable thermodynamics for the Fe₂O₃–TiO₂ system. Moreover, deposition of isolated Fe(III)-oxo clusters by atomic layer deposition (ALD) [53] and recently by wet impregnation and post-thermal decomposition of Fe acetylacetonate precursors onto TiO₂ [54], resulted in enhanced VLA reactivity for organic dye degradation and the oxygen evolution reaction during water splitting, respectively. Decoration of high-quality ALD-fabricated TiO₂ inverse opals by Fe₂O₃ nanoparticles using a post-hydrothermal treatment resulted in substantial improvement of the photocurrent density under UV-vis illumination related to the enhanced visible light absorption and reduced electron-hole recombination in Fe₂O₃–TiO₂ [58]. Very recently, surface modification of TiO₂ PC films by CoO_x nanoclusters using the CCC method led to a marked performance amplification for organics photocatalytic decomposition at low CoO_x loadings associated with the beneficial combination of slow-photon-assisted visible light trapping with the increased charge separation in CoO_x–TiO₂ inverse opal films [59].

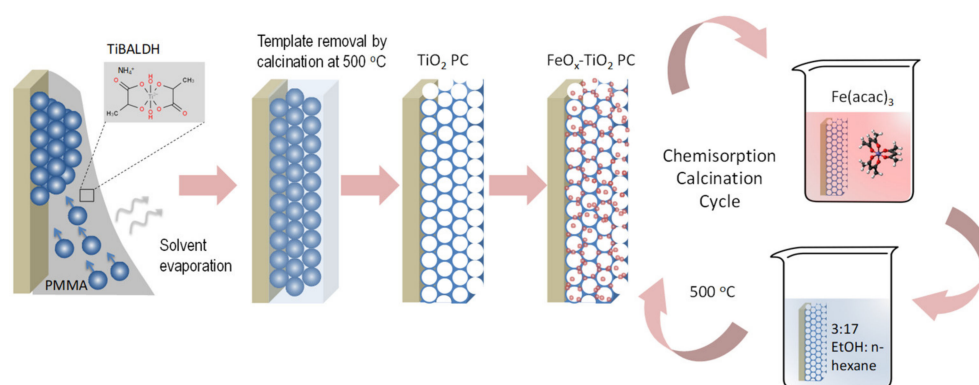
In this work, surface deposition of nanoscale FeO_x on TiO₂ PC films is systematically investigated in order to exploit synergistic effects of PC-assisted visible light trapping and improved charge separation in FeO_x–TiO₂ photocatalytic films. TiO₂ inverse opal films were deposited by the co-assembly of variable diameter colloidal sphere templates and a hydrolyzed TiO₂ precursor and then surface modified by successive CC cycles using Fe(III) acetylacetonate, which allowed the controlled variation of FeO_x loading on PBG engineered TiO₂ PCs. Deposition of low amounts of FeO_x nanoclusters on TiO₂ inverse opals resulted in the selective improvement of photocatalytic degradation of salicylic acid and photocurrent density under visible light, surpassing similarly modified P25 films

and evading the loss of holes oxidizing ability that is usually observed in VLA TiO₂ photocatalysts. The observed enhancement was related to the synergy of light trapping and surface states induced by the interfacial coupling between TiO₂ and FeO_x. However, increasing iron oxide loading competed with the photonic enhancement, especially under UV-Vis illumination due to the persistent surface recombination by defect d-states.

2. Materials and Methods

2.1. Materials Fabrication

TiO₂ inverse opals of variable PBGs were fabricated by the convective evaporation-induced co-assembly of polymer microspheres with titanium(IV) bis(ammonium lactato)dihydroxide (TIBALDH) sol-gel precursor (Scheme 1) [60,61].



Scheme 1. Deposition process for co-assembled FeO_x-TiO₂ inverse opals.

Specifically, colloidal dispersions of monodisperse polymer spheres of different diameters, namely 220 nm polystyrene (PS) spheres (Polysciences Inc., 8% CV, SD = 0.02 μm, 2.7 % solids *w/v*) and poly (methyl methacrylate)-PMMA spheres with diameters of 260 nm (Microparticles GmbH, 2.4% CV, SD = 0.006 μm, 5.0 % solids *w/v*) and 330 nm (Polysciences Inc., <5% CV, SD = 0.019 μm, 2.5% solids *w/v*), were used to tune the photonic films PBG across the FeO_x-TiO₂ electronic absorption edge. Glass slides cleaned in Hellmanex (Hellmanex III, Helma Analytics, Müllheim, Germany), followed by ultrasound sonication in acetone and ethanol (EtOH), were nearly vertically suspended in a beaker containing 10 mL of 0.1 wt.% dilute sphere suspension and 0.056 mL of fresh titania precursor prepared by mixing 0.25 mL of 50 wt.% aqueous TIBALDH solution (388165, Sigma-Aldrich, St. Louis, MO, USA), 0.5 mL of 0.1 M HCl, and 1 mL EtOH. The beakers were kept at 55 °C until the solvent fully evaporated, leading to self-assembled films containing the titania gel within the opal interstices. The films were then calcined at 500 °C for 2 h in the air (1 °C/min), to remove the colloidal template and crystallize titania inverse opals. The pristine TiO₂ PC films were labeled as PC220, PC260, and PC330 after the templating sphere diameter.

Surface modification of the titania inverse opal by iron oxides was implemented using as precursor salt the iron(III) acetylacetonate complex, Fe(acac)₃ (12534, Alfa Aesar Thermo Fisher Scientific, Heysham, Lancashire, UK) for the CCC technique (Scheme 1). The PC films were immersed for 24 h at room temperature in a volatile 6.5 × 10⁻⁴ M Fe(acac)₃ solution prepared from 23 mg Fe(acac)₃ diluted in 100 mL of solvent consisting of 15 mL EtOH and 85 mL normal hexane (ethanol: n-hexane = 3:17 *v/v*) [56]. Copious rinsing of the impregnated films with the solvent was used to remove physisorbed Fe(acac)₃ molecules, followed by calcination in the air (1 °C/min) at 500 °C for 1 h to remove organic species and allow the formation of stable FeO_x-TiO₂ composites via Fe-O-Ti interfacial bonds [57]. The CC treatment was repeated up to three times for the best performing PC260 inverse opals. The corresponding films were labeled as FeO_x-PCXXX-nth, where XXX = 220, 260, and 330 is the template sphere diameter and n is the CC cycle index.

Mesoporous titania films were spin-coated on cleaned glass substrates using a paste of titania nanopowder (Aeroxide[®] P25, Evonik, Essen, Germany) [59] as a benchmark

reference to validate the photonic films' activity. After post-annealing at 450 °C in the air to remove organic species, the P25 films were surface modified using Fe(acac)₃ under identical conditions, and the corresponding films were labeled as FeO_x-P25-nth according to the CCC cycle index.

2.2. Characterization

The materials' morphological and structural properties were investigated by an FEI scanning electron microscope (SEM) (Quanta Inspect, FEI, Eindhoven, The Netherlands) equipped with an energy-dispersive X-ray analyzer (EDX) (EDXDX4, Mahwah, NJ, USA). The structure and phase composition of the PC films were studied by a transmission electron microscope (TEM, CM20, FEI, Eindhoven, The Netherlands) coupled with energy-filtered TEM (GIF 200, Gatan, Pleasanton, CA, USA) and an FEI Talos F200i field-emission scanning transmission electron microscope (Thermo Fisher Scientific Inc., Waltham, MA, USA) operating at 200 kV, equipped with a windowless energy-dispersive spectroscopy microanalyzer (6T/100 Bruker, Hamburg, Germany). The films' structural properties were also investigated by micro-Raman spectroscopy (inVia Reflex, Renishaw, London, UK) using the 514 nm line of an Ar⁺ ion laser. The laser beam was focused onto the films by a ×100 objective (NA = 0.90), while the laser power was controlled at low-density levels (<0.1 mW/μm²) to evade local heating. X-ray photoelectron spectroscopy (XPS) was performed on a PHOIBOS 100 (SPECS, Berlin, Germany) hemispherical analyzer using Mg-Kα (1253.6 eV) X-ray source (SPECS XR50). The spectrometer was calibrated on clean Ag, Cu, and Au samples for which the Ag 3d_{5/2}, Cu 2p_{3/2}, and Au 4f_{7/2} peak positions were determined at 368.3, 932.7, and 84 eV, respectively. The XPS spectra were collected at a 52° take-off angle using a pass energy of 7 eV. The adventitious C 1s set to 284.8 eV was used for charge referencing. Fitting was performed using XPS Peak Fit and Shirley background subtraction. Photoluminescence (PL) measurements were carried out using the focused beam of a 275 nm light-emitting diode as excitation, while the PL signal was collected through a long-pass 320 nm filter by a fiber optic spectrometer (LR1, ASEQ Instruments, Vancouver, Canada). The optical properties were investigated by diffuse and specular reflectance measurements using a fiber-optic diffuse and a 15° specular reflectance accessory on a Cary60 UV-Vis spectrometer, respectively. A Halon reference and a UV-enhanced Al mirror were used for background determination. Attenuated total reflection Fourier-transform infrared (ATR-FTIR) spectra were recorded on a JASCO 470Plus (JASCO Corp., Hachioji, Tokyo, Japan) FT-IR spectrometer equipped with a PIKE MIRacle ATR accessory using a single reflection diamond/ZnSe crystal plate.

Photoelectrochemical measurements were performed in a three-electrode configuration using a CS350 potentiostat/galvanostat (Wuhan Corrtest Instruments Corp., Ltd., Wuhan, China), Ag/AgCl as a reference, and a Pt foil as counter electrodes. The working photoelectrode was prepared by depositing the PC and P25 films on cleaned fluorine-doped tin oxide (FTO) conductive glass substrates (7 ohms/sq, Sigma-Aldrich, St. Louis, MO, USA) followed by FeO_x surface modification using the CCC method. The electrolyte was 0.5 M NaOH, while UV-Vis and illumination were provided by a 300 W Xe lamp (120 mW/cm²) combined with a long pass 400 nm cutoff filter for visible light selection. Electrochemical impedance spectroscopy (EIS) measurements were performed at an open-circuit voltage (V_{OC}), in the 10⁴–10^{−1} Hz frequency range with 10 mV ac amplitude.

2.3. Photocatalytic Performance

Photocatalytic activity evaluation for the PC and P25 films was carried out on the aqueous phase degradation of salicylic acid (SA) under UV-Vis and Vis illumination. Films of 2 cm² area were initially stirred in vials containing 3 mL of 30 μM SA aqueous solution for 30 min under dark in order to reach adsorption-desorption equilibrium. The solution pH was fixed at 3 by dilute HCL in order to enhance SA adsorption on the TiO₂ films [33]. A 150 W Xe lamp was used as a UV-Vis light source along with a heat-reflective mirror (20CLVS-3, Newport, Irvine, CA, USA), while visible light was selected by a

400 nm cutoff filter. The horizontal light beam was directed on the films using a UV-enhanced Al mirror at 100 mW/cm^2 power density. Aliquots of 0.5 mL were periodically taken out from the SA solution and analyzed in the spectrophotometer using a 10 mm path length quartz microcell. Additional photocatalytic tests were performed in the presence of $5 \mu\text{M}$ isopropanol (IPA) and formic acid as hydroxyl radical and hole scavengers, respectively. The photocatalytic tests were repeated three times and standard errors were derived for the mean kinetic constants.

3. Results and Discussion

3.1. Structural and Optical Properties

Co-assembly of the TIBALDH precursor with the sacrificial colloidal polymer spheres resulted in the formation of well-ordered inverse opal structures consisting of the (111) planes of an fcc crystal lattice of void spheres, as shown by the SEM images of Figure 1a–c, distinctly different from the rough, aggregated morphology of mesoporous P25 films (Figure 1d). The hexagonally ordered macropores of the inverse opals structure were interconnected through smaller ones (dark areas within the large spherical voids) that form after calcination at the contact points of neighboring polymer spheres facilitating mass transfer in the pore network. Their mean diameter (D) determined by SEM, increased proportionally to the colloidal sphere size (Table 1), while the obtained values were about 60% smaller than those of the templating spheres because of the persistent volume contraction of crystalline metal oxide inverse opals [33,60]. Cross-section SEM images revealed that the thickness of the inverse opal films was approximately $4 \mu\text{m}$ (Figure 1e), while that for the P25 film was approximately $2.2 \mu\text{m}$ (Figure 1f). The P25 films will accordingly have considerably higher, by ca. 50%, titania mass loading compared to the photonic ones, assuming identical wall mesoporosity and an ideal solid filling factor of 0.26 for the inverse opals. The presence of PBG was identified by specular reflectance ($R\%$) measurements for all the photonic films at 15° incidence (Figure 1g). A clear $R\%$ peak due to Bragg reflection was invariably observed for all PCs at wavelengths increasing with the inverse opal diameter (Table 1), characteristic for the incomplete PBG (stopband) formation along the [111] direction in titania inverse opal structures [26].

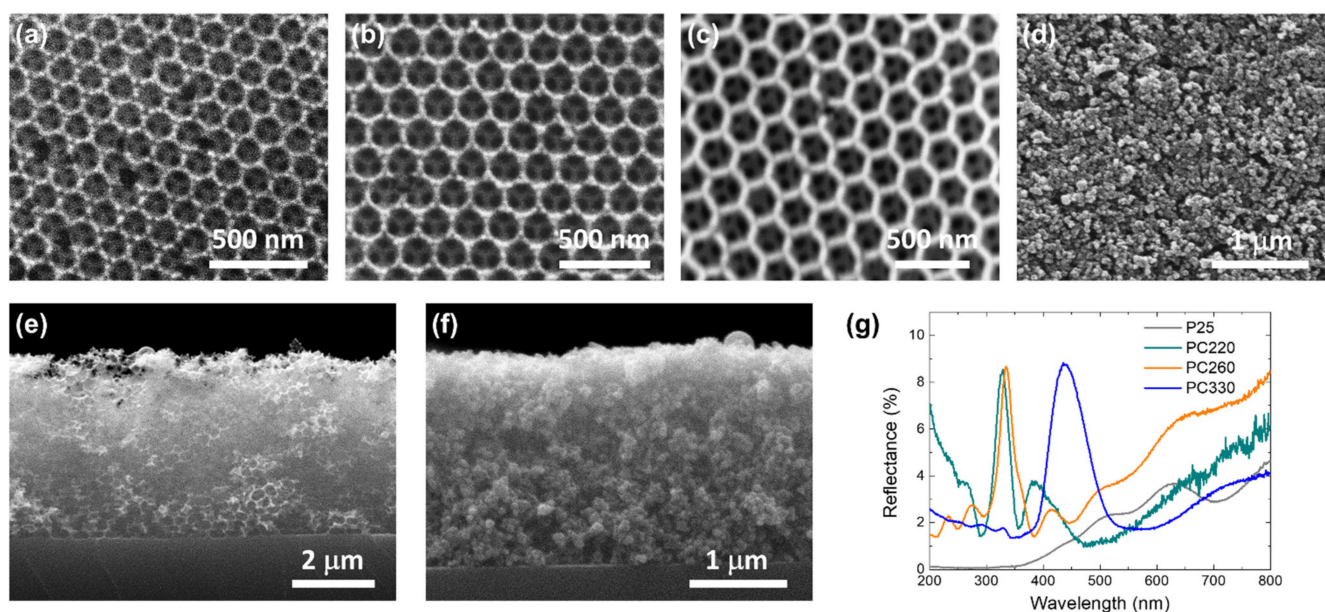


Figure 1. Top-view SEM images of (a) PC220, (b) PC260, (c) PC330 TiO₂ inverse opals in comparison with the (d) mesoporous P25 films. Cross-sections of (e) PC260 and (f) P25 films. (g) Specular reflectance ($R\%$) of the PC and P25 films at 15° incidence angle.

Table 1. Optical parameters for the TiO₂ inverse opal films.

Sample	D^a (nm)	$\lambda_{\text{exp}}(15^\circ)^b$ (Air)	n_{eff} (Air)	$1-f$	n_{eff} (H ₂ O)	$\lambda(0^\circ)^c$ (Air)	$\lambda(0^\circ)^c$ (H ₂ O)
PC220	135	325	1.50	0.22	1.68	330	371
PC260	150	335	1.39	0.17	1.60	341	393
PC330	200	437	1.36	0.16	1.58	445	517

^a D = inverse opal macropore diameter determined from SEM. ^b $\lambda_{\text{exp}}(15^\circ)$ = stop band wavelength determined from R% spectra at 15° incidence angle. ^c $\lambda(0^\circ)$ = stop band wavelength according to the modified Bragg law at 0° incidence angle.

The stopband variation for the different inverse opals contrasts the Fabry-Pérot interference fringes most clearly observed for the mesoporous P25 films at wavelengths exceeding titania's electronic absorption edge at $\lambda > 400$ nm. It should be noted that the amplitude of the Bragg peak was relatively low (<10%) for all co-assembled photonic films reflecting the presence of submillimeter-sized PC domains interrupted by cracks within the coarse spot of the measuring beam (1–2 mm²) used in the R% measurements [32], which lead to enhanced diffuse scattering especially toward the low-energy PBG edge (vide infra) and possibly the increase of R% below 260 nm, most prominent for PC220. Applying modified Bragg's law for first-order diffraction from the (111) fcc planes (Supplementary material S1) yielded the effective refractive index n_{eff} and the corresponding solid filling fraction $1 - f$ ($f = 0.74$ for the fcc lattice) in the air (Table 1) based on the experimental $\lambda_{\text{exp}}(15^\circ)$ values and the inverse opal diameters D . The obtained values for $1 - f$ were appreciably smaller than the theoretical one of 0.26 for complete filling of the inverse fcc lattice, corroborating the formation of mesoporous nanocrystalline walls in the co-assembled TiO₂ inverse opal [62]. Furthermore, using the derived filling fractions and the water refractive index ($n_{\text{H}_2\text{O}} = 1.33$), the PBG positions were estimated for the inverse opals in water (Table 1), where the aqueous phase photocatalytic reaction is carried out.

Surface modification of the TiO₂ films by successive CC cycles of Fe(acac)₃ had no observable effect either on the PCs' periodicity and macropore diameter or the P25 film morphology, as shown in Figure S1. The deposition of Fe species was verified by EDX elemental analysis using the Ti K and Fe K peaks for the CCC surface-modified TiO₂ films. Quantification indicated that the Fe loading amount increased continuously with the number of cycles, as shown in Table S1. Comparison between the different photonic films showed that the PC220 films presenting the smallest macropore diameter exhibited slightly higher Fe (at%) uptake. This complies with the higher surface area and mesopore volume reported for co-assembled TiO₂ PC films with small macropores increasing the available interfaces between skeletal walls [59].

The phase composition of the surface-modified inverse opals was studied by TEM, as shown in Figure 2. TEM images for FeO_x-PC260-1st (Figure 2a–c) showed the presence of mesoporous walls consisting of aggregated nanoparticles (<10 nm) in the anatase TiO₂ phase. The latter was identified by the most intense diffraction spots from the (101), (004), (200) planes with corresponding d-spacings of 0.35, 0.24, and 0.19 nm, as shown by the fast Fourier transform (FFT) patterns in the inset of Figure 2b. Moreover, dark inclusions of 1–3 nm could be discerned among the anatase nanoparticles, with no distinct FFT pattern that could be related to iron oxides. These nanoscale deposits, whose crystallinity could not be resolved, point to the presence of ultrafine FeO_x species, complying with a recent thorough study on the immobilization of MO co-catalysts, including FeO_x, on TiO₂ using the Fe(acac)₃ precursor [44]. Moreover, local EDX spectral analysis in the TEM image of FeO_x-PC260-1st (Figure 2c) verified the presence of Fe species, as shown in Figure 2d. Energy filtered TEM (EFTEM) analysis was additionally carried out in order to trace the location and distribution of FeO_x species on the nanocrystalline anatase walls of the FeO_x-PC260-3rd films with the highest Fe loading amount (Figure 2e–h).

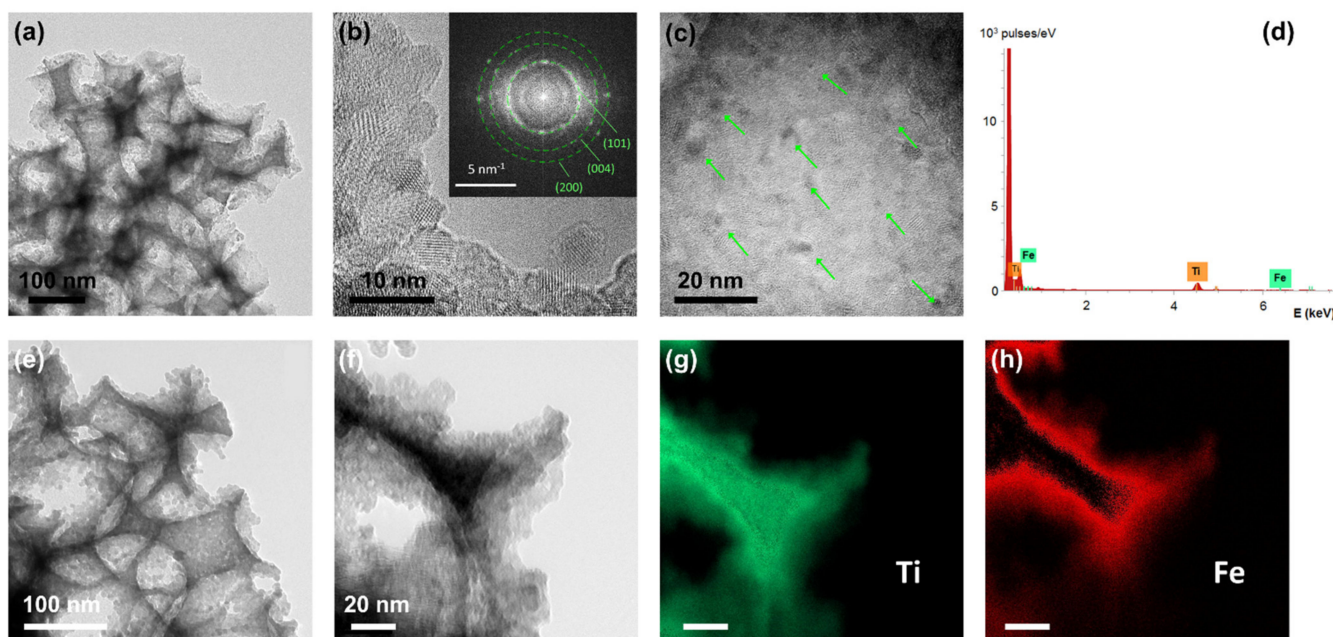


Figure 2. (a–c) TEM images for FeO_x-PC260-1st at different magnifications. The inset in (b) shows the corresponding FFT pattern (d) Local EDX spectrum corresponding to the image (b). (e,f) TEM images for FeO_x-PC260-3rd at different magnifications and the (g) Ti and (h) Fe EFTEM elemental maps corresponding to (f).

Ti and Fe elemental maps obtained for the area depicted in the TEM image of Figure 2f showed the decoration of the TiO₂ inverse opal skeleton with Fe species, indicating that both dispersed FeO_x nanoclusters, as well as their aggregates, are deposited in FeO_x-PC-3rd films.

The surface composition of the FeO_x-PC films was further investigated by XPS. Figure 3a shows the characteristic Ti 2p spin-orbit doublets for the pristine and FeO_x-PC260 inverse opals after the 1st and 3rd CC cycle. Close fitting of the experimental peaks could be obtained for both pristine and FeO_x-modified PC260 films using two distinct components at 458.23 eV with full-width at half-maximum (FWHM) of ~1.3 eV and 463.93 eV with FWHM~2.1 eV, respectively. The Ti 2p_{1/2}-Ti 2p_{3/2} splitting was 5.7 eV, indicating the presence of Ti⁴⁺ ions and stoichiometric TiO₂ [63] with no observable contribution of lower Ti oxidation after surface modification with Fe(acac)₃. Moreover, the Fe 2p_{3/2} and 2p_{1/2} core level peaks in Figure 3b verified the formation of iron species in the FeO_x-modified PC260 films. The Fe 2p_{3/2} peak curve fitting showed contributions from both Fe⁺² and Fe⁺³ species at 709.3 eV and 711.2 eV respectively. The Fe⁺² satellite peak was also identified at 714.4 eV, about 5.1 eV above the Fe⁺² main peak as expected for ferrous compounds [64]. The presence of both Fe²⁺ and Fe³⁺ oxidation states is accordingly inferred for the FeO_x-modified PC films, in agreement with previous reports [44,56], with a significant contribution from Fe²⁺ oxides such as FeO and Fe(OH)₂, which are known to be prone to non-stoichiometry and oxidation, respectively [65].

The structural and compositional properties of the photonic and P25 films before and after FeO_x modification were further studied by Raman spectroscopy at 514 nm excitation. The Raman spectra for the bare PC films presented the characteristic vibrational modes of nanocrystalline anatase TiO₂ at approximately 147 (E_g), 198 (E_g), 399 (B_{1g}), 518 (A_{1g} + B_{1g}), and 641 cm⁻¹ (E_g) [66], as shown in Figure S2. No Raman bands due to polymer and carbonaceous species or other TiO₂ phases could be detected, indicating the growth of single-phase anatase TiO₂ PC films after thermal treatment at 500 °C. Substantial blue-shifts and spectral broadening of the Raman bands though, were detected, especially for the most intense low-frequency mode, compared to the P25 films (inset of Figure S2).

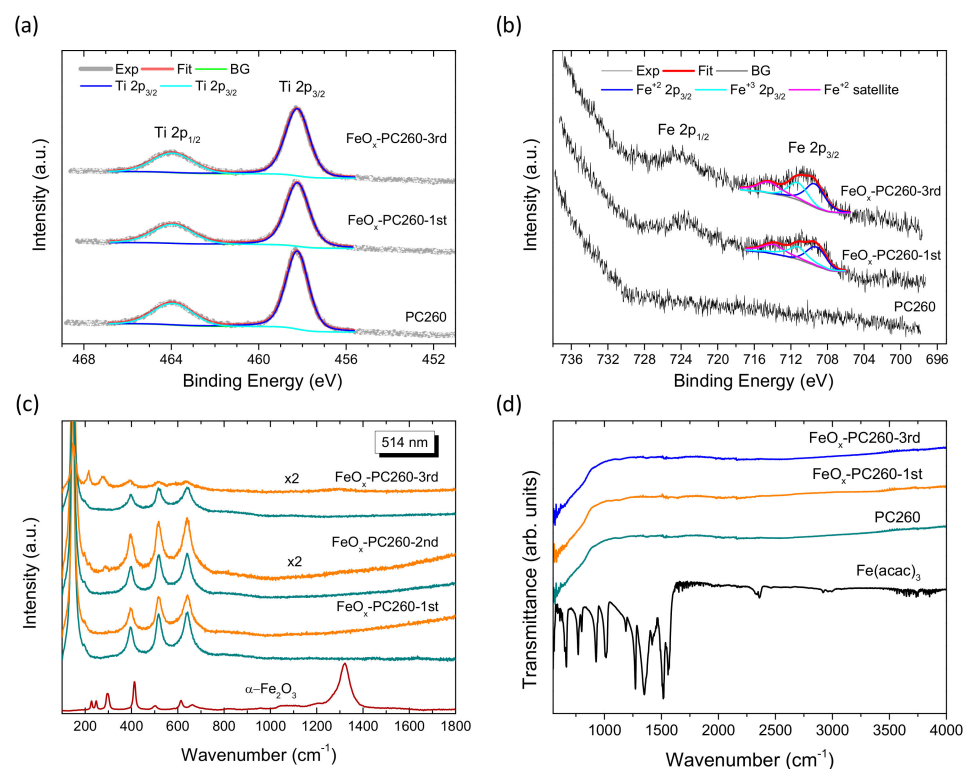


Figure 3. (a) Ti 2p and (b) Fe 2p core level for the pristine and surface modified FeO_x -PC260 films after the 1st and 3rd CC cycle. Solid lines correspond to the total fit and the individual peaks of the Ti 2p and Fe $2p_{3/2}$ spectral deconvolution. (c) Raman spectra of the FeO_x -PC260 films for the different CC cycles before (green) and after (orange) laser annealing in comparison with a reference hematite spectrum at 514 nm. (d) ATR-FTIR spectra of the neat $\text{Fe}(\text{acac})_3$ precursor, PC260, and FeO_x -PC260 after the 1st and 3rd CC cycles.

This behavior can be associated with the breakdown of the $q = 0$ selection rule and the presence of sub-10 nm anatase nanocrystallites in the TiO_2 photonic films [66], in perfect agreement with the high resolution-TEM analysis and recent Raman results corroborating the partial inhibition of anatase growth in co-assembled TiO_2 inverse opals using the TiBALDH precursor [32,59].

No additional Raman bands due to iron oxides could be traced after CCC modification by $\text{Fe}(\text{acac})_3$ on either the PC (Figure 3c) or P25 (Figure S3) films, even though excitation at 514 nm (2.41 eV) approaches closely the absorption edge of most iron oxides [65] and thus it is expected to be highly sensitive to the films' surface composition by means of resonance Raman scattering [47]. To explore the presence of FeO_x on the CCC modified films, local annealing experiments were performed by focusing the 514 nm laser beam on the FeO_x -PC260 (Figure 3c) and FeO_x -P25 (Figure S3) films by the $100\times$ objective at full laser power (2.5 mW) for 60 s in order to investigate the local oxidation of FeO_x nanoclusters to stable iron oxide phases. Normal Raman spectra were then recorded on the same spot using low laser power density ($0.05 \text{ mW}/\mu\text{m}^2$) to trace any local phase transformation. A series of new Raman peaks indeed emerged at approximately 215, 277, and 1310 cm^{-1} for the photonic FeO_x -PC260-2nd and FeO_x -PC260-2nd films (Figure 3c) and from the first CC cycle for FeO_x -P25 (Figure S3). These Raman bands are close to the characteristic Raman modes of hematite $\alpha\text{-Fe}_2\text{O}_3$ [67], as shown in the reference spectra of Figure S4a [68]. They could be identified during laser heating experiments on maghemite ($\gamma\text{-Fe}_2\text{O}_3$) nanoparticles, as shown in Figure S4b, while the same laser-induced transformation to hematite has been previously reported for the less crystalline ferrihydrite and wüstite phases [67,69]. These results suggest that poorly crystallized or even amorphous FeO_x nanoclusters are deposited on the anatase walls of the surface-modified PC films, consistent with the TEM-

EDX and XPS results. This was further corroborated by comparative ATR-FTIR spectra on FeO_x-PC260 films with respect to the individual constituents, as shown in Figure 3d. No observable IR mode from the different iron oxides and oxyhydroxides [65] could be traced in the studied frequency range (550–4000 cm⁻¹) after thermal treatment at 500 °C. It should be noted that Fe(II) oxides i.e., FeO, Fe(OH)₂, and the mixed-valence Fe₃O₄ are not expected to produce strong IR bands in this spectral range [65], especially when these oxides are poorly crystallized. These results comply with the recent report on the amorphous state of MO_x species on surface-modified TiO₂ by wet impregnation-post calcination of metal acetylacetonate precursors, regardless of the calcination protocol [44].

Figure 4 compares the diffuse reflectance spectra of the FeO_x-modified inverse opal and mesoporous titania films. An intense DR% band was clearly observed at 336 nm for PC220, while broader ones were resolved at about 350 and 455 nm for PC260 and PC330, respectively. These bands followed closely the corresponding Bragg R% peaks of the PC films (Figure 1g), while they were distinctively different from the absorption edge of anatase at 375 nm and the corresponding DR% spectrum of P25 films (Figure 4d), whose absorption edge was red-shifted by about 20 nm with respect to the PC films due to small amounts of rutile nanoparticles that possess a lower (~3.0 eV) bandgap. Moreover, the DR% bands of the PC films were systematically red-shifted by 6–10 nm with respect to the corresponding $\lambda(0^\circ)$ values (Table 1). This behavior can be related to the enhanced diffuse scattering at the low-energy (red) edge of the PC stop band, where slow photons localize mainly in the high refractive index anatase inverse opal frame [32]. Surface modification by FeO_x nanoclusters resulted in the decrease of DR% intensity below 500–600 nm, most clearly detected for the FeO_x-PC260 and FeO_x-P25 films that were subjected up to three CC cycles. The corresponding FeO_x-P25 absorbance spectra derived from the Kubelka-Munk transform with no interference from Bragg reflection (Figure S5), showed the progressive extension of electronic absorption for FeO_x-TiO₂, reaching 500 nm after the 3rd CC cycle, due to the contribution of iron oxides. This effect was likewise observed for the CCC-modified PC films together with the continuous drop of stopband reflection arising from the increased FeO_x visible light absorption.

3.2. Photocatalytic Activity

The photocatalytic performance evaluation for the FeO_x-modified PC and P25 films was carried out on the degradation of SA, a colorless water pollutant, which, unlike dyes, absorbs at $\lambda < 330$ nm (Figure S6a), well below the PCs' stop bands in water, and thus precludes any photonic enhancement by means of slow photon spectral overlap with the SA absorbance [32]. In addition, the photocatalytic tests were performed at acidic pH = 3, which favors chemisorption of SA molecules on titania and their preferential oxidation by valence band holes [33,70], providing a first indication for the oxidation power of visible light-generated holes in the FeO_x-TiO₂ films. Control experiments in the absence of either PC or P25 films, indicated weak SA degradation under both visible and UV-Vis light, while the continuous decrease of the SA concentration (C) was observed with time in the presence of the photocatalytic films, as shown in Figure S6b,c. For all samples, the $\ln(C/C_0)$ vs. t plots, with C_0 being the initial SA concentration after dark adsorption, varied linearly with time under both visible (Figure 5a) and UV-Vis light (Figure S6d), indicating that SA photodegradation followed pseudo-first-order kinetics. The apparent kinetic constants k_{vis} and $k_{\text{UV-Vis}}$ were accordingly determined from the slopes of the linear $\ln(C/C_0)$ vs. t plots and the corresponding reaction rates were then calculated as $r = kC_0$ for low (<mM) pollutant concentrations [32] in order to determine the films' activity independently of C_0 variations due to SA adsorption. The PC220 and PC260 films showed rather weak SA photodegradation under visible light that decreased further for PC330. This small VLA photocatalytic activity can be related to either unintentional doping effects in the pristine PCs and/or weak UVA radiation leakage from the filtered Xe lamp source in combination with slow light trapping effects at the anatase absorption edge, which have been amply identified for TiO₂ PCs under UV-Vis light [18,26].

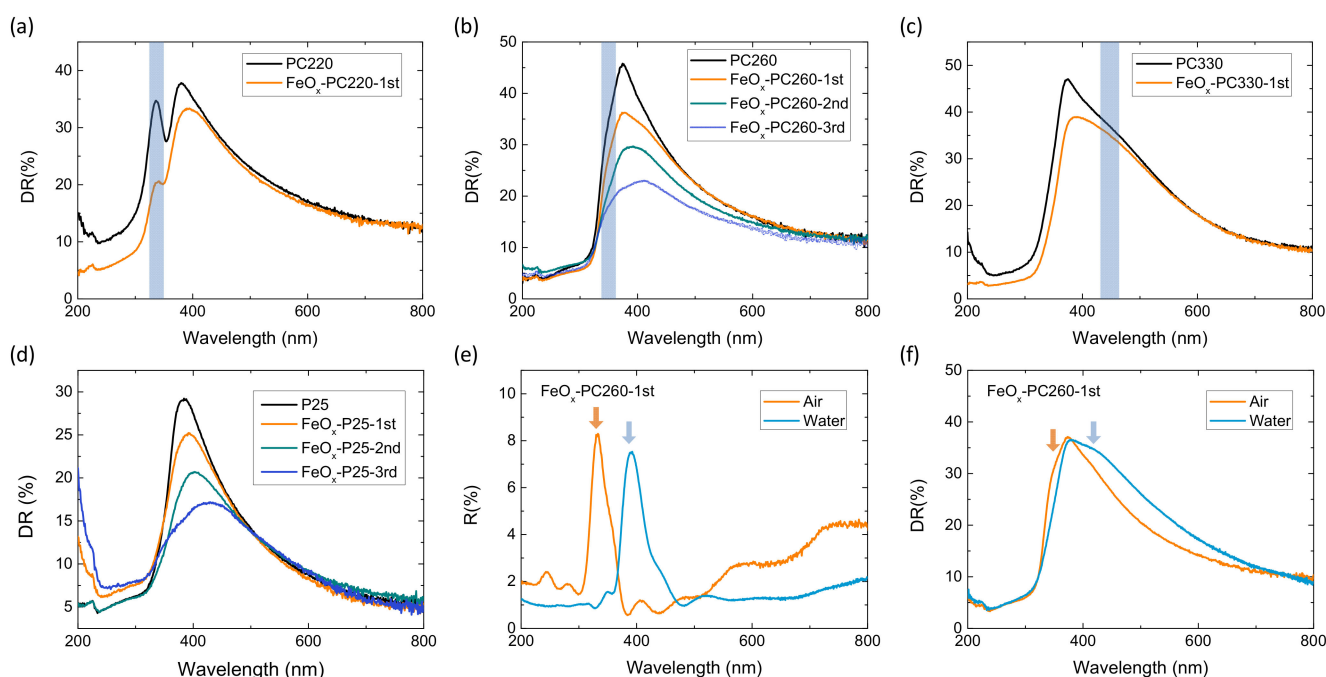


Figure 4. Diffuse reflectance spectra for the (a) PC220, (b) PC260, (c) PC330, and (d) P25 films before and after FeO_x CCC modification. Shaded bands denote the positions of the DR% Bragg reflectance for the PC films. Comparative (e) diffuse and (f) specular reflectance spectra for FeO_x-PC260-1st films in air and water.

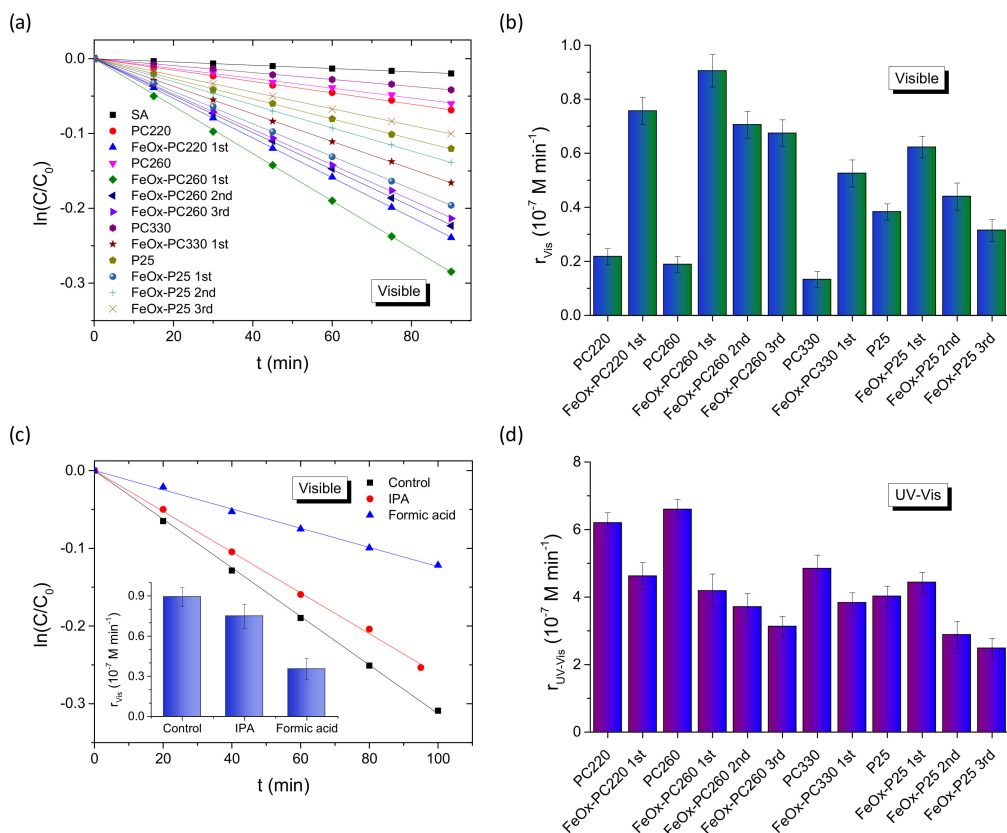


Figure 5. (a) SA photodegradation kinetics for the FeO_x-modified PC and P25 films under visible light and (b) the corresponding reaction rates r_{vis} . (c) SA degradation kinetics for FeO_x-PC260-1st in the presence of IPA and formic acid as hydroxyl radical and hole scavengers, respectively. (d) The reaction rates r_{UV-Vis} for the FeO_x-modified PC and P25 films under UV-Vis light.

Specifically, TiO₂ inverse opals with low-energy stopband edges approaching titania's electronic absorption edge present marked improvements of the photocatalytic rates due to red-edge slow-photons, while detrimental Bragg reflection is suppressed by titania's bandgap absorbance. This amplification effect has been recently identified for co-assembled TiO₂ PCs opals on SA degradation under UV-Vis light [33], in perfect agreement with the present results for the unmodified photonic films in Figure 5d. A further shift of the PC's stopband to the visible range by the increase of macropore size such as PC330, leads to the drop of photocatalytic activity due to the absence of any electronic absorption as well as the decrease of the films' surface area, which in the case of self-assembled TiO₂ inverse opals is largely determined by the mesopores in the nanocrystalline skeleton walls that increase for the smaller macropore diameters [59]. On the other hand, the bare mesoporous P25 films exceeded significantly the PCs' performance, mainly due to the presence of rutile nanocrystals, whose narrower electronic bandgap of about 3.0 eV and the interfacial charge transfer from rutile to the anatase nanoparticles underlie their VLA photocatalytic activity [71].

FeO_x surface modification resulted invariably in marked improvements of r_{vis} for all CC-modified TiO₂ films (Figure 5b), especially after the 1st CC cycle, with the inverse opals outperforming the benchmark mesoporous FeO_x-P25 films (by about 45% after the 1st CC cycle) in spite of their higher catalyst mass. Moreover, the obtained r_{vis} rates depended distinctively on the macropore diameter of the inverse opals (Figure 5b), indicating significant differences in the light-harvesting ability of the PC films. Specifically, FeO_x-PC260-1st exhibited the highest r_{vis} , followed closely by FeO_x-C220-1st, whereas the larger diameter FeO_x-PC330-1st presented the lowest activity (by about 75%). This size dependence can be closely associated with the PC's stopband variation and the concomitant slow photon amplification effects, most prominent for PC260, whose stopband is expected at ~393 nm in water (Table 1). Assuming that the PBG's spectral width is about the FWHM \approx 30 nm of the Bragg R% peak (Figure 1c) [62], the PC260's stopband in water is expected at 393 ± 15 nm and the corresponding red-edge slow photons, which span a narrower spectral range of about 20 nm [18], will occur roughly within 410–430 nm, matching closely the electronic absorption of FeO_x nanoclusters (Figure S5). This behavior was directly identified by R% measurements for the FeO_x-PC260-1st films in water (Figure 4e), where the red-shift of the specular R% peak at λ_{exp} (15°) by about 60 cm^{-1} was directly confirmed complying with the predictions of modified Bragg's law (Table 1). A larger red-shift of the broad DR% peak in water from about 350 (air) to 420 cm^{-1} (water) was also observed (Figure 4f) reflecting closely the spectral shift of the red-slow photon region that matches the FeO_x electronic absorption range. The slow photon region is expected to blue-shift by about 20 nm for PC220 (Table 1), i.e., in the range of 390–410 nm, leading to a smaller spectral overlap with FeO_x absorbance at $\lambda > 400$ nm, applied for the visible light photocatalytic experiments. On the other hand, no appreciable slow-photon effects are expected for the larger diameter FeO_x-PC330-1st, whose stop band in water at about 517 nm (Table 1) is well above FeO_x absorbance after the 1st CC cycle for appreciable blue-edge slow photon effects.

To investigate the oxidation power of photogenerated holes in the visible light degradation mechanism of SA, comparative photocatalytic tests were performed for the best performing FeO_x-PC260-1st in the presence of IPA and formic acid as hydroxyl radical and hole scavengers, respectively (Figure 5c). In the former case, a relatively small decrease of r_{vis} by 16% was observed, while a marked drop by 61% was detected in the case of formic acid, indicating that holes generated in the FeO_x-TiO₂ films under visible light are the main reactive oxygen species for SA decomposition. However, an increase of FeO_x loading for both PC260 and P25 films after consecutive 2nd and 3rd cycles resulted in the systematic drop of r_{vis} (Figure 5b), despite the increase of visible light absorbance detected in the corresponding DR% spectra (Figure 5b,d). This behavior may be partly associated with the formation of FeO_x aggregates on the nanocrystalline anatase walls (Figure 2h) that will impair the FeO_x-TiO₂ interfacial charge transfer as well as the suppression of photonic enhancement effects by the increased FeO_x absorption that impedes light propagation in

the PC structure [72]. This detrimental effect was significantly aggravated in the case of UV-Vis illumination (Figure 5d), where FeO_x surface modification resulted in the decrease of $r_{\text{UV-Vis}}$ from the 1st cycle for the PCs, followed by a continuous drop for subsequent CC cycles. A small increase of $r_{\text{UV-Vis}}$ was detected for the FeO_x -P25 films (by about 10%) after the 1st CC cycle, followed by an appreciable decrease after the 2nd and 3rd CC cycles. This behavior indicates that besides absorption losses for higher FeO_x loading that inhibit photonic amplification effects and deteriorate the VLA photocatalytic performance of PC films, additional reasons underlie the decline of photocatalytic performance in the FeO_x - TiO_2 system. In fact, similar behavior was earlier reported for Fe_xO_y -P25 nanocomposites [53], where, the presence of low amounts of isolated Fe(III)-oxo clusters on the surface of TiO_2 nanoparticles resulted in significant photocatalytic activity and hydroxyl radical formation under visible light. However, the UV photocatalytic rates were comparatively lower than those of the pristine P25 nanoparticles, indicating that Fe(III) oxo-centers on TiO_2 may act as trapping sites that moderate the composite's oxidation power.

3.3. Charge Separation

To investigate charge separation in the FeO_x -PC films, photoelectrochemical measurements were performed under visible and UV-Vis irradiation. Photocurrent transients for the CCC-modified PC260 films under chopped visible light illumination at 0.2 V vs. Ag/AgCl (Figure 6a) showed an appreciable increase for both the instantaneous (hole current) and steady-state photocurrent for FeO_x -PC260-1st compared to the pristine PC260, reflecting the enhanced visible light-harvesting of the modified PC films for low FeO_x contents. However, the photocurrent densities decreased progressively for FeO_x -PC260-2nd and FeO_x -PC260-3rd despite their higher visible light absorbance caused by the increase of FeO_x loading. This behavior, which mirrors closely the corresponding variation of the r_{Vis} rates on SA photodegradation, indicates that surface recombination contributes largely to the films' performance decrease, especially after the 2nd and 3rd CC cycles [73].

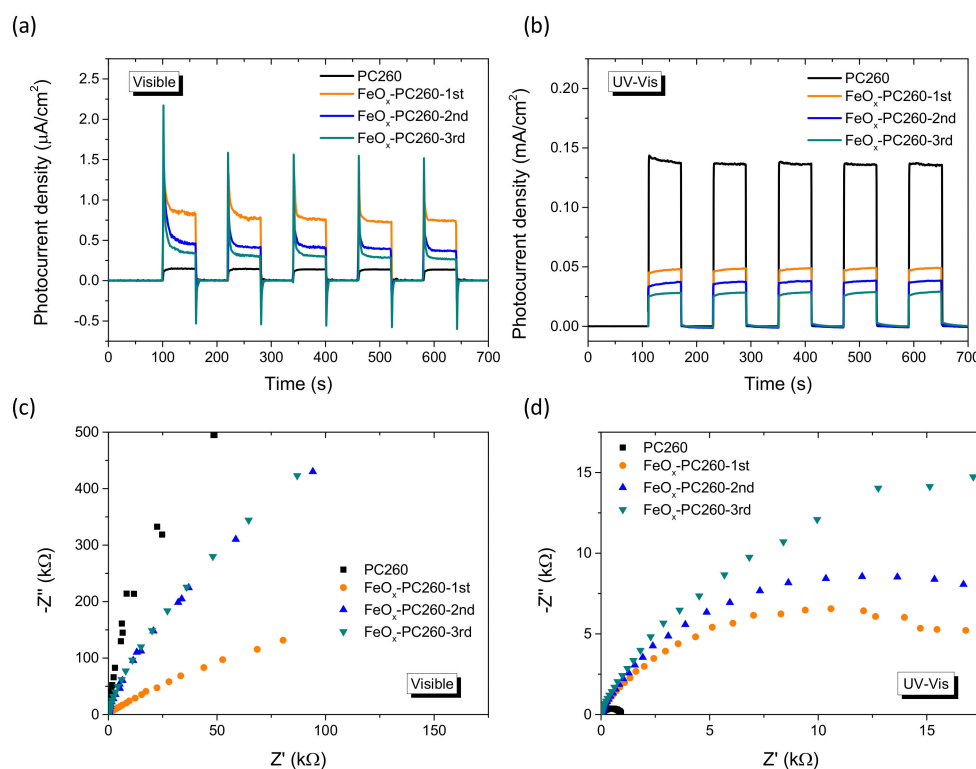


Figure 6. Transient photocurrents under chopped light and EIS Nyquist plots for (a,c) visible and (b,d) UV-Vis illumination for the FeO_x -PC260 films.

On the other hand, the photocurrents decreased continuously with FeO_x loading under UV-Vis irradiation (Figure 6b), pointing to reduced UV oxidation power of FeO_x -PC films, alike SA photodegradation experiments. This effect was supported by EIS measurements on the FeO_x -PC260 films under both visible and UV-Vis irradiation. Comparative Nyquist plots (Figure 6c) showed that the radius of the capacitive arc at higher frequencies in the EIS plane decreased for FeO_x -PC260-1st compared to the pristine PC260 and increased after the 2nd and 3rd CC cycles under visible light, indicative of reduced charge transfer resistance for the 1st CC cycle. On the other hand, the opposite behavior was observed under UV-Vis light, where impedance and the corresponding arc radius increased consecutively for the FeO_x -PC260 films, indicating that FeO_x nanoclusters on the nanocrystalline TiO_2 inverse opal walls may create surface traps that compromise the materials' oxidation power under UV-Vis light.

Charge recombination and the presence of defect states were explored by PL spectroscopy for the FeO_x -PC260 films under 275 nm excitation, as shown in Figure 7a. The PL spectrum of pristine PC260 showed a broadband at 380 nm arising from the near-band gap emission via indirect band-to-band transitions of anatase nanoparticles, accompanied by a much weaker shoulder at about 450 nm originating from shallow defect states due to oxygen vacancies [5,74,75]. Surface modification by FeO_x nanoclusters resulted in the progressive decrease of near-band gap emission along with a red shift of its spectral position reaching 400 nm for FeO_x -PC260-3rd. These features comply favorably with the interfacial electron transfer and the rise of the composite's valence band (VB) maximum by means of a FeO_x -induced surface d-band above the anatase valence band edge, respectively (Figure 7b). In addition, the broad defect-induced PL emission at 450 nm was gradually enhanced for the FeO_x -PC260 films after the 1st and 2nd CC cycles, indicating the increase of radiative recombination via shallow FeO_x -induced states below the anatase conduction band (CB) edge [56,57]. Such vacant surface d-states have been shown to lie close to those of pristine anatase and the reduction potential of O_2/O_2^- ($E^0 = -0.33$ V vs. NHE) allowing superoxide radical formation by trapped photogenerated electrons without impeding the photocatalytic activity of CCC-modified TiO_2 under optimal loading of FeO_x nanoclusters [37]. However, a broad distribution of these defect states can be assumed in the present case because of the mixed-phase composition of FeO_x nanoclusters (Figure 7b), which will be further expanded with the increase of FeO_x loading and aggregation. Defect states at variable energies straddling the O_2/O_2^- reduction potential may then increase surface recombination under UV-Vis excitation, since trapped electrons at states more negative than $E^0(\text{O}_2/\text{O}_2^-)$ will recombine resulting in the observed increase of defect-induced PL emission (Figure 7b) and the higher recombination kinetics probed by EIS under UV-Vis light. On the other hand, the persistent recombination via these defect states under visible light, cannot completely suppress charge separation in the FeO_x - TiO_2 system that sustains appreciable VLA photocatalytic performance at low FeO_x loading amounts, which is further assisted by visible light trapping in the PBG engineered inverse opals.

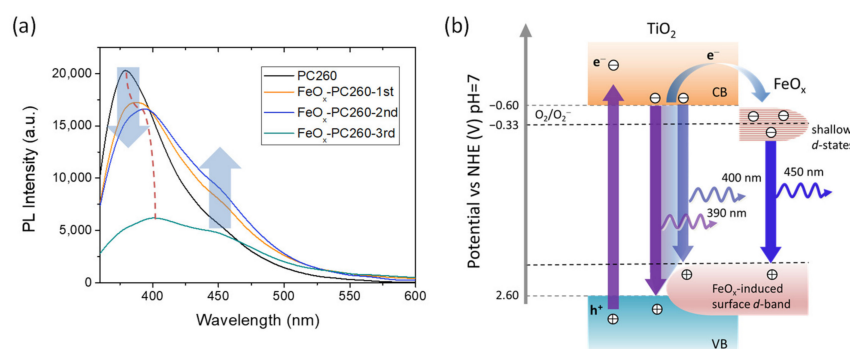


Figure 7. (a) PL spectra of the CCC-modified PC260 films and (b) schematic depicting the emission processes in FeO_x -PC under UV excitation. The anatase band edge positions were taken from [76].

4. Conclusions

Surface modification of co-assembled TiO₂ inverse opals by variable amounts of FeO_x nanoclusters was implemented by successive chemisorption-calcination cycles of Fe(III) acetylacetonates on the nanocrystalline anatase PC walls, leading to composite FeO_x-TiO₂ photonic films with extended visible light absorption. PBG engineering of the co-assembled inverse opals across the composite FeO_x-TiO₂ absorption edge was performed by tuning the templating colloidal spheres size. Distinctive diameter-dependent improvements of the SA photocatalytic degradation rates and photocurrent density were thus obtained under visible light for low loading amounts of FeO_x nanoclusters, which outperformed benchmark P25 films subjected to the same treatment. Scavenger experiments indicated that holes generated in the FeO_x-TiO₂ films under visible light are the major reactive oxygen species for SA decomposition, evading the weak oxidizing power of photogenerated holes frequently met in VLA TiO₂ photocatalysts. The observed performance amplification was related to the improved charge separation induced by the interfacial coupling between TiO₂ and FeO_x in combination with optimal light trapping by red-edge slow photons resonating with the FeO_x-TiO₂ absorption edge. However, an increase in FeO_x loading resulted in the drastic drop of photocatalytic performance mainly because of a broad distribution of defect d-states straddling the O₂/O₂⁻ reduction potential that increase surface recombination according to photoelectrochemical and PL experiments. Fine-tuning of heterostructured metal oxide PC photocatalysts' composition is concluded to be a key factor for the fabrication of efficient VLA photocatalytic films with enhanced visible light trapping and charge separation.

Supplementary Materials: The following are available online at <https://www.mdpi.com/article/10.3390/ma14237117/s1>, Figure S1: Top view SEM images of pristine and FeO_x modified PC260 and P25 films by two consecutive CC cycles of Fe(acac)₃, Table S1: Elemental EDX analysis of the FeO_x-modified PC and P25 films, Figure S2: Raman spectra for the pristine and CCC modified PC and P25 films at 514 nm, Figure S3: Raman spectra for the FeO_x-P25 films (thick lines) at 514 nm before and after local annealing experiments, Figure S4: Reference Raman spectra of representative iron oxides at 514 nm and Raman spectra acquired on maghemite (γ-Fe₂O₃) nanoparticles after local laser annealing experiments at variable laser power densities, Figure S5: Kubelka-Munk transform function F(R) obtained from the DR (%) of the FeO_x-P25 films, Figure S6: SA absorbance spectra in the presence of FeO_x-PC260-1st and SA photodegradation kinetics under visible and UV-Vis light illumination for the pristine and FeO_x-modified PC and P25 films.

Author Contributions: Conceptualization, V.L.; methodology, V.L. and A.T.; formal analysis, M.P., A.T., E.S. and E.X.; investigation, M.P., A.T., E.S., E.X., S.G., N.B. and A.D.; resources, V.L.; N.B.; A.D. and S.G.; writing—original draft preparation, M.P.; writing—review and editing, V.L.; M.P. and A.T.; supervision, V.L. All authors have read and agreed to the published version of the manuscript.

Funding: The research work was supported by the Hellenic Foundation for Research and Innovation (H.F.R.I.) under the “First Call for H.F.R.I. Research Projects to support Faculty members and Researchers and the procurement of high-cost research equipment grant” (Project Number: 543).

Institutional Review Board Statement: Not applicable.

Informed Consent Statement: Not applicable.

Data Availability Statement: Not applicable.

Acknowledgments: We would like to thank Dimitrios Palles for his kind assistance with the micro-Raman measurements.

Conflicts of Interest: The authors declare no conflict of interest.

References

1. Etacheri, V.; Di Valentin, C.; Schneider, J.; Bahnemann, D.; Pillai, S.C. Visible-light activation of TiO₂ photocatalysts: Advances in theory and experiments. *J. Photochem. Photobiol. Photochem. Rev.* **2015**, *25*, 1–29. [[CrossRef](#)]
2. Xu, C.; Ravi Anusuyadevi, P.; Aymonier, C.; Luque, R.; Marre, S. Nanostructured materials for photocatalysis. *Chem. Soc. Rev.* **2019**, *48*, 3868–3902. [[CrossRef](#)]

3. Wang, Q.; Domen, K. Particulate photocatalysts for light-driven water splitting: Mechanisms, challenges, and design strategies. *Chem. Rev.* **2020**, *120*, 919–985. [[CrossRef](#)] [[PubMed](#)]
4. Fujishima, A.; Zhang, X.; Tryk, D.A. TiO₂ photocatalysis and related surface phenomena. *Surf. Sci. Rep.* **2008**, *63*, 515–582. [[CrossRef](#)]
5. Lettieri, S.; Pavone, M.; Fioravanti, A.; Santamaria Amato, L.; Maddalena, P. Charge carrier processes and optical properties in TiO₂ and TiO₂-based heterojunction photocatalysts: A review. *Materials* **2021**, *14*, 1645. [[CrossRef](#)]
6. Banerjee, S.; Pillai, S.C.; Falaras, P.; O'Shea, K.E.; Byrne, J.; Dionysiou, D.D. New insights into the mechanism of visible light photocatalysis. *J. Phys. Chem. Lett.* **2014**, *5*, 2543–2554. [[CrossRef](#)] [[PubMed](#)]
7. Kumaravel, V.; Mathew, S.; Bartlett, J.; Pillai, S.C. Photocatalytic hydrogen production using metal doped TiO₂: A review of recent advances. *Appl. Catal. B Environ.* **2019**, *244*, 1021–1064. [[CrossRef](#)]
8. Meng, X.; Liu, L.; Ouyang, S.; Xu, H.; Wang, D.; Zhao, N.; Ye, J. Nanometals for solar-to-chemical energy conversion: From semiconductor-based photocatalysis to plasmon-mediated photocatalysis and photo-thermocatalysis. *Adv. Mater.* **2016**, *28*, 6781–6803. [[CrossRef](#)]
9. Wei, Z.; Janczarek, M.; Wang, K.; Zheng, S.; Kowalska, E. Morphology-governed performance of plasmonic photocatalysts. *Catalysts* **2020**, *10*, 1070. [[CrossRef](#)]
10. Bai, S.; Jiang, J.; Zhang, Q.; Xiong, Y. Steering charge kinetics in photocatalysis: Intersection of materials syntheses, characterization techniques and theoretical simulations. *Chem. Soc. Rev.* **2015**, *44*, 2893–2939. [[CrossRef](#)]
11. Kubacka, A.; Caudillo-Flores, U.; Barba-Nieto, I.; Fernandez-García, M. Towards full-spectrum photocatalysis: Successful approaches and materials. *Appl. Catal. A General* **2011**, *610*, 117966. [[CrossRef](#)]
12. Papailias, I.; Todorova, N.; Giannakopoulou, T.; Ioannidis, N.; Boukos, N.; Athanasekou, C.P.; Dimotikali, D.; Trapalis, C. Chemical vs. thermal exfoliation of g-C₃N₄ for NO_x removal under visible light irradiation. *Appl. Catal. B Environ.* **2018**, *239*, 16–26. [[CrossRef](#)]
13. Ge, J.; Zhang, Y.; Park, S.-J. Recent advances in carbonaceous photocatalysts with enhanced photocatalytic performances: A mini review. *Materials* **2019**, *12*, 1916. [[CrossRef](#)] [[PubMed](#)]
14. Von Freymann, G.; Kitaev, V.; Lotsch, B.V.; Ozin, G.A. Bottom-up assembly of photonic crystals. *Chem. Soc. Rev.* **2013**, *42*, 2528–2554. [[CrossRef](#)] [[PubMed](#)]
15. Yang, C.; Liu, L.; Zhu, S.; Yu, Z.; Xi, X.; Wu, S.; Cao, H.; Li, J.; Zhao, L. GaN with laterally aligned nanopores to enhance the water splitting. *J. Phys. Chem. C* **2017**, *121*, 7331–7336. [[CrossRef](#)]
16. Yang, C.; Xi, X.; Yu, Z.; Cao, H.; Li, J.; Lin, S.; Ma, Z.; Zhao, L. Light modulation and water splitting enhancement using a composite porous GaN structure. *ACS Appl. Mater. Interfaces* **2018**, *10*, 5492–5497. [[CrossRef](#)]
17. Lim, S.Y.; Law, C.S.; Markovic, M.; Marsal, L.F.; Voelcker, N.H.; Abell, A.D.; Santos, A. Rational management of photons for enhanced photocatalysis in structurally-colored nanoporous anodic alumina photonic crystals. *ACS Appl. Energy Mater.* **2019**, *2*, 1169–1184. [[CrossRef](#)]
18. Chen, J.I.L.; von Freymann, G.; Choi, S.Y.; Kitaev, V.; Ozin, G.A. Amplified photochemistry with slow photons. *Adv. Mater.* **2006**, *18*, 1915–1919. [[CrossRef](#)]
19. Zhang, X.; John, S. Enhanced photocatalysis by light-trapping optimization in inverse opals. *J. Mater. Chem. A* **2020**, *8*, 18974–18986. [[CrossRef](#)]
20. El Harakeh, M.; Halaoui, L. Enhanced conversion of light at TiO₂ photonic crystals to the blue of a stop band and at TiO₂ random films sensitized with Q-CdS: Order and disorder. *J. Phys. Chem. C* **2010**, *114*, 2806–2813. [[CrossRef](#)]
21. Li, X.; Yang, C.; Li, J.; Xi, X.; Ma, Z.; Lin, S.; Zhao, L. Controllable fabrication of lateral periodic nanoporous GaN and its enhance photocatalytic water splitting performance. *Appl. Surf. Sci.* **2020**, *526*, 146618. [[CrossRef](#)]
22. Li, X.; Hu, T.; Lin, S.; Ma, Z.; Wang, J.; Zhao, L. Fabrication of layer-ordered porous GaN for photocatalytic water splitting. *Int. J. Hydrogen Energy* **2021**, *46*, 7878–7884. [[CrossRef](#)]
23. Lim, S.Y.; Hedrich, C.; Jiang, L.; Law, C.S.; Abell, A.D.; Blick, R.H.; Zierold, R.; Santos, A. Harnessing slow light in optoelectronically engineered nanoporous photonic crystals for visible light-enhanced photocatalysis. *ACS Catal.* **2021**, *11*, 12947–12962. [[CrossRef](#)]
24. Stein, A.; Wilson, B.E.; Rudisill, S.G. Design and functionality of colloidal-crystal-templated materials-chemical applications of inverse opals. *Chem. Soc. Rev.* **2013**, *42*, 2763–2803. [[CrossRef](#)] [[PubMed](#)]
25. Phillips, K.R.; England, G.T.; Sunny, S.; Shirman, E.; Shirman, T.; Vogel, N.; Aizenberg, J.A. Colloidoscope of colloid-based porous materials and their uses. *Chem. Soc. Rev.* **2016**, *45*, 281–322. [[CrossRef](#)] [[PubMed](#)]
26. Likodimos, V. Photonic crystal-assisted visible light activated TiO₂ photocatalysis. *Appl. Catal. B Environ.* **2018**, *230*, 269–303. [[CrossRef](#)]
27. Lu, Y.; Yu, H.; Chen, S.; Quan, X.; Zhao, H. Integrating plasmonic nanoparticles with TiO₂ photonic crystal for enhancement of visible-light-driven photocatalysis. *Environ. Sci. Technol.* **2012**, *46*, 1724–1730. [[CrossRef](#)]
28. Cai, Z.; Xiong, Z.; Lu, X.; Teng, J. In situ gold-loaded titania photonic crystals with enhanced photocatalytic activity. *J. Mater. Chem. A* **2014**, *2*, 545–553. [[CrossRef](#)]
29. Collins, G.; Lonergan, A.; McNulty, D.; Glynn, C.; Buckley, D.; Hu, C.; O'Dwyer, C. Semiconducting metal oxide photonic crystal plasmonic photocatalysts. *Adv. Mater. Interfaces* **2020**, *7*, 3908–3920. [[CrossRef](#)]
30. Raja-Mogan, T.; Ohtani, B.; Kowalska, E. Photonic crystals for plasmonic photocatalysis. *Catalysts* **2020**, *10*, 827. [[CrossRef](#)]

31. Boppella, R.; Kochuveedu, S.T.; Kim, H.; Jeong, M.J.; Mota, F.M.; Park, J.H.; Kim, D.H. Plasmon-sensitized graphene/TiO₂ inverse opal nanostructures with enhanced charge collection efficiency for water splitting. *ACS Appl. Mater. Interfaces* **2017**, *9*, 7075–7083. [[CrossRef](#)]
32. Diamantopoulou, A.; Sakellis, E.; Romanos, G.E.; Gardelis, S.; Ioannidis, N.; Boukos, N.; Falaras, P.; Likodimos, V. Titania photonic crystal photocatalysts functionalized by graphene oxide nanocolloids. *Appl. Catal. B Environ.* **2019**, *240*, 277–290. [[CrossRef](#)]
33. Apostolaki, M.-A.; Toumazatou, A.; Antoniadou, M.; Sakellis, E.; Xenogiannopoulou, E.; Gardelis, S.; Boukos, N.; Falaras, P.; Dimoulas, A.; Likodimos, V. Graphene quantum dot-TiO₂ photonic crystal films for photocatalytic applications. *Nanomaterials* **2020**, *10*, 2566. [[CrossRef](#)] [[PubMed](#)]
34. Zhang, K.; Liu, Y.; Deng, J.; Xie, S.; Lin, H.; Zhao, X.; Yang, J.; Han, Z.; Dai, H. Fe₂O₃/3DOM BiVO₄: High-performance photocatalysts for the visible light-driven degradation of 4-nitrophenol. *Appl. Catal. B Environ.* **2017**, *202*, 569–579. [[CrossRef](#)]
35. Huang, J.; Chu, D.; Li, K.; Li, X.; Liu, A.; Zhang, C.; Du, Y.; Yang, P. TiO₂ photonic crystal sensitized with Mn₃O₄ nanoparticles and porphine manganese(III) as efficient photoanode for photoelectrochemical water splitting. *J. Phys. Chem. C* **2018**, *122*, 260–266. [[CrossRef](#)]
36. Loukopoulos, S.; Toumazatou, A.; Sakellis, E.; Xenogiannopoulou, E.; Boukos, E.; Dimoulas, A.; Likodimos, V. Heterostructured CoO_x-TiO₂ mesoporous/photonic crystal bilayer films for enhanced visible-light harvesting and photocatalysis. *Materials* **2020**, *13*, 4305. [[CrossRef](#)]
37. Tada, H.; Jin, Q.; Iwaszuk, A.; Nolan, M. Molecular-scale transition metal oxide nanocluster surface-modified titanium dioxide as solar-activated environmental catalysts. *J. Phys. Chem. C* **2014**, *118*, 12077–12086. [[CrossRef](#)]
38. Maeda, K.; Ishimaki, K.; Okazaki, M.; Kanazawa, T.; Lu, D.; Nozawa, S.; Kato, H.; Kakihana, M. Cobalt oxide nanoclusters on rutile titania as bifunctional units for water oxidation catalysis and visible light absorption: Understanding the structure–activity relationship. *ACS Appl. Mater. Interfaces* **2017**, *9*, 6114–6122. [[CrossRef](#)] [[PubMed](#)]
39. Liu, J.; Ke, J.; Li, Y.; Liu, B.; Wang, L.; Xiao, H.; Wang, S. Co₃O₄ quantum dots/TiO₂ nanobelt hybrids for highly efficient photocatalytic overall water splitting. *Appl. Catal. B Environ.* **2018**, *236*, 396–403. [[CrossRef](#)]
40. Okazaki, M.; Wang, Y.; Yokoi, T.; Maeda, K. Visible-light driven water oxidation using anatase titania modified with first row transition-metal-oxide nanoclusters. *J. Phys. Chem. C* **2019**, *123*, 10429–10434. [[CrossRef](#)]
41. Tanaka, H.; Uchiyama, T.; Kawakami, N.; Okazaki, M.; Uchimoto, Y.; Maeda, K. Water oxidation through interfacial electron transfer by visible light using cobalt-modified rutile titania thin-film photoanode. *ACS Appl. Mater. Interfaces* **2020**, *12*, 9219–9225. [[CrossRef](#)] [[PubMed](#)]
42. Ran, J.; Zhang, J.; Yu, J.; Jaroniec, M.; Qiao, S.Z. Earth-abundant cocatalysts for semiconductor-based photocatalytic water splitting. *Chem. Soc. Rev.* **2014**, *43*, 7787–7812. [[CrossRef](#)] [[PubMed](#)]
43. Šuligoj, A.; Arčon, I.; Mazaj, M.; Dražič, G.; Arčon, D.; Cool, P.; Štangar, U.L.; Tušar, N.N. Surface modified titanium dioxide using transition metals: Nickel as a winning transition metal for solar light photocatalysis. *J. Mater. Chem. A* **2018**, *6*, 9882–9892. [[CrossRef](#)]
44. Schubert, J.S.; Popovic, J.; Haselmann, G.M.; Nandan, S.P.; Wang, J.; Giesriegl, A.; Cherevan, A.S.; Eder, D. Immobilization of Co, Mn, Ni and Fe oxide co-catalysts on TiO₂ for photocatalytic water splitting reactions. *J. Mater. Chem. A* **2019**, *7*, 18568–18579. [[CrossRef](#)]
45. AlSalka, Y.; Granone, L.I.; Ramadan, W.; Hakki, A.; Dillert, R.; Bahnemann, D.W. Iron-based photocatalytic and photoelectrocatalytic nano-structures: Facts, perspectives, and expectations. *Appl. Catal. B Environ.* **2019**, *244*, 1065–1095. [[CrossRef](#)]
46. Sivula, K.; Le Formal, F.; Grätzel, M. Solar water splitting: Progress using hematite (α-Fe₂O₃) photoelectrodes. *ChemSusChem* **2014**, *4*, 432–449. [[CrossRef](#)] [[PubMed](#)]
47. Kontos, A.I.; Likodimos, V.; Stergiopoulos, T.; Tsoukleris, D.S.; Falaras, P.; Rabias, I.; Papavassiliou, G.; Kim, D.; Kunze, J.; Schmuki, P. Self-organized anodic TiO₂ nanotube arrays functionalized by iron oxide nanoparticles. *Chem. Mater.* **2009**, *21*, 662–672. [[CrossRef](#)]
48. Wodka, D.; Socha, R.P.; Bielanska, E.; Elzbiaciak-Wodka, M.; Nowak, P.; Warszynski, P. Photocatalytic activity of titanium dioxide modified by Fe₂O₃ nanoparticles. *Appl. Surf. Sci.* **2014**, *319*, 173–180. [[CrossRef](#)]
49. Rtimi, S.; Pulgarin, C.; Sanjines, R.; Kiwi, J. Novel FeO_x-polyethylene transparent films: Synthesis and mechanism of surface regeneration. *RSC Adv.* **2015**, *5*, 80203–80211. [[CrossRef](#)]
50. Ganeshraja, A.S.; Rajkumar, K.; Zhu, K.; Li, X.; Thirumurugan, S.; Xu, W.; Zhang, J.; Yang, M.; Anbalagan, K.; Wang, J. Facile synthesis of iron oxide coupled and doped titania nanocomposites: Tuning of physicochemical and photocatalytic properties. *RSC Adv.* **2016**, *6*, 72791–72802. [[CrossRef](#)]
51. Surówka, M.; Kobielski, M.; Trochowski, M.; Buchalska, M.; Kruczała, K.; Broś, P.; Macyk, W. Iron and other metal species as phase-composition controllers influencing the photocatalytic activity of TiO₂ materials. *Appl. Catal. B Environ.* **2019**, *247*, 173–181. [[CrossRef](#)]
52. Soltys-Mroz, M.; Syrek, K.; Pierzchala, J.; Wiercigroch, E.; Malek, K.; Sulka, G.D. Band gap engineering of nanotubular Fe₂O₃-TiO₂ photoanodes by wet impregnation. *Appl. Surf. Sci.* **2020**, *517*, 146195. [[CrossRef](#)]
53. Libera, J.A.; Elam, J.W.; Sather, N.F.; Rajh, T.; Dimitrijevic, N.M. Iron(III)-oxo centers on TiO₂ for visible-light photocatalysis. *Chem. Mater.* **2010**, *22*, 409–413. [[CrossRef](#)]

54. Rtimi, S.; Pulgarin, C.; Nadtochenko, V.A.; Gostev, F.E.; Shelaev, I.V.; Kiwi, J. FeO_x-TiO₂ film with different microstructures leading to femtosecond transients with different properties: Biological implications under visible light. *Sci. Reps.* **2016**, *6*, 30113–30123. [[CrossRef](#)] [[PubMed](#)]
55. Serpone, N.; Maruthamuthu, P.; Pichat, P.; Pelizzetti, E.; Hidaka, H. Exploiting the interparticle electron transfer process in the photocatalysed oxidation of phenol, 2-chlorophenol and pentachlorophenol: Chemical evidence for electron and hole transfer between coupled semiconductors. *J. Photochem. Photobiol. A Chem.* **1995**, *85*, 247–255. [[CrossRef](#)]
56. Tada, H.; Jin, Q.; Nishijima, H.; Yamamoto, H.; Fujishima, M.; Okuoka, S.-I.; Hattori, T.; Sumida, Y.; Kobayashi, H. Titanium(IV) dioxide surface-modified with iron oxide as a visible light photocatalyst. *Angew. Chem. Int. Ed.* **2011**, *50*, 3501–3505. [[CrossRef](#)] [[PubMed](#)]
57. Jin, Q.; Fujishima, M.; Tada, H. Visible-light-active iron oxide modified anatase titanium(IV) dioxide. *J. Phys. Chem. C* **2011**, *115*, 6478–6483. [[CrossRef](#)]
58. Liu, J.; Sun, C.; Fu, M.; Long, J.; He, D.; Wang, Y. Enhanced photochemical catalysis of TiO₂ inverse opals by modification with ZnO or Fe₂O₃ using ALD and the hydrothermal method. *Mater. Res. Express* **2018**, *5*, 025509. [[CrossRef](#)]
59. Toumazatou, A.; Antoniadou, M.; Sakellis, E.; Tsoutsou, D.; Gardelis, S.; Romanos, G.E.; Ioannidis, N.; Boukos, N.; Dimoulas, A.; Falaras, P.; et al. Boosting visible light harvesting and charge separation in surface modified TiO₂ photonic crystal catalysts by CoO_x nanoclusters. *Mater. Adv.* **2020**, *1*, 2310–2322. [[CrossRef](#)]
60. Hatton, B.; Mishchenko, L.; Davis, S.; Sandhage, K.H.; Aizenberg, J. Assembly of large-area, highly ordered, crack-free inverse opal films. *Proc. Natl. Acad. Sci. USA* **2010**, *107*, 10354–10359. [[CrossRef](#)] [[PubMed](#)]
61. Cai, Z.; Liu, Y.J.; Teng, J.; Lu, X. Fabrication of large domain crack-free colloidal crystal heterostructures with superposition bandgaps using hydrophobic polystyrene spheres. *ACS Appl. Mater. Interfaces* **2012**, *4*, 5562–5569. [[CrossRef](#)] [[PubMed](#)]
62. Papadakis, D.; Diamantopoulou, A.; Pantazopoulos, P.A.; Palles, D.; Sakellis, E.; Boukos, N.; Stefanou, N.; Likodimos, V. Nanographene oxide-TiO₂ photonic films as plasmon-free substrates for surface-enhanced Raman scattering. *Nanoscale* **2019**, *11*, 21542–21553. [[CrossRef](#)]
63. Biesinger, M.C.; Lau, L.W.M.; Gerson, A.R.; Smart, R.S.C. Resolving surface chemical states in XPS analysis of first row transition metals, oxides and hydroxides: Sc, Ti, V, Cu and Zn. *Appl. Surf. Sci.* **2010**, *257*, 887–898. [[CrossRef](#)]
64. Grosvenor, A.P.; Kobe, B.A.; Biesinger, M.C.; McIntyre, N.S. Investigation of multiplet splitting of Fe 2p XPS spectra and bonding in iron compounds. *Surf. Interface Anal.* **2004**, *36*, 1564–1574. [[CrossRef](#)]
65. Cornell, R.M.; Schwertmann, U. Characterization. In *The Iron Oxides: Structure, Properties, Reactions, Occurrences and Uses*; Wiley-VCH Verlag GmbH & Co. KGaA: Weinheim, Germany, 2003.
66. Balaji, S.; Djaoued, Y.; Robichaud, J. Phonon confinement studies in nanocrystalline anatase-TiO₂ thin films by micro-Raman spectroscopy. *J. Raman Spectrosc.* **2006**, *37*, 1416–1422. [[CrossRef](#)]
67. De Faria, D.L.A.; Silva, S.V.; de Oliveira, M.T. Raman microspectroscopy of some iron oxides and oxyhydroxides. *J. Raman Spectrosc.* **1997**, *28*, 873–878. [[CrossRef](#)]
68. Molchan, S.; Thompson, G.E.; Lindsay, R.; Skeldon, P.; Likodimos, V.; Romanos, G.E.; Falaras, P.; Adamova, G.; Iliev, B. Corrosion behaviour of mild steel in 1-alkyl-3-methylimidazolium tricyanomethanide ionic liquids for CO₂ capture applications. *RSC Adv.* **2014**, *4*, 5300–5311. [[CrossRef](#)]
69. Varadwaj, K.S.K.; Panigrahi, M.K.; Ghose, J. Effect of capping and particle size on Raman laser-induced degradation of γ-Fe₂O₃ nanoparticles. *J. Solid State Chem.* **2004**, *177*, 4286–4292. [[CrossRef](#)]
70. Tunesi, S.; Anderson, M. Influence of chemisorption on the photodecomposition of salicylic acid and related compounds using suspended TiO₂ ceramic membranes. *J. Phys. Chem.* **1991**, *95*, 3399–3405. [[CrossRef](#)]
71. Likodimos, V.; Chrysi, A.; Calamiotou, M.; Fernández-Rodríguez, C.; Doña-Rodríguez, J.M.; Dionysiou, D.D.; Falaras, P. Microstructure and charge trapping assessment in highly reactive mixed phase TiO₂ photocatalysts. *Appl. Catal. B Environ.* **2016**, *192*, 242–252. [[CrossRef](#)]
72. Von Freymann, G.; John, S.; Schulz-Dobrick, M.; Vekris, E.; Tetreault, N.; Wong, S.; Kitaev, V.; Ozin, G.A. Tungsten inverse opals: The influence of absorption on the photonic band structure in the visible spectral region. *Appl. Phys. Lett.* **2004**, *84*, 224–226. [[CrossRef](#)]
73. Dunn, H.K.; Feckl, J.M.; Müller, A.; Fattakhova-Rohlfing, D.; Morehead, S.G.; Roos, J.; Peter, L.M.; Scheu, C.; Bein, T. Tin doping speeds up hole transfer during lightdriven water oxidation at hematite photoanodes. *Phys. Chem. Chem. Phys.* **2014**, *16*, 24610–24620. [[CrossRef](#)] [[PubMed](#)]
74. Serpone, N.; Lawless, D.; Khairutdinov, R. Size effects on the photophysical properties of colloidal anatase TiO₂ particles: Size quantization versus direct transitions in this indirect semiconductor? *J. Phys. Chem.* **1995**, *99*, 16646–16654. [[CrossRef](#)]
75. Toyoda, T.; Yindeesuk, W.; Okuno, T.; Akimoto, M.; Kamiyama, K.; Hayase, S.; Shen, Q. Electronic structures of two types of TiO₂ electrodes: Inverse opal and nanoparticulate cases. *RSC Adv.* **2015**, *5*, 49623–49632. [[CrossRef](#)]
76. Beranek, R.; Kisch, H. Tuning the optical and photoelectrochemical properties of surface-modified TiO₂. *Photochem. Photobiol. Sci.* **2008**, *7*, 40–48. [[CrossRef](#)] [[PubMed](#)]